Cryogenics 113 (2021) 103207

Contents lists available at ScienceDirect

Cryogenics

journal homepage: www.elsevier.com/locate/cryogenics

Research paper

High-speed density measurement for LNG and other cryogenic fluids using electrical capacitance tomography

Andrew Hunt [a,*], Ijhar Rusli [a], Menne Schakel [b], Asaad Kenbar [c]

[a] Coventry University, FCS Research Centre, Coventry CV1 2NL, UK
[b] VSL Dutch Metrology Institute, Thijsseweg 11, 2629 JA Delft, the Netherlands
[c] TÜV SÜD National Engineering Laboratory, Scottish Enterprise Technology Park, Reynolds Ave, Glasgow G75 0QF, UK

ARTICLE INFO

Keywords:
Liquified natural gas
LNG
Electrical capacitance tomography
ECT
Density measurement

ABSTRACT

The global custody transfer market for liquefied natural gas (LNG) has grown at a strong pace in the last decade and use of LNG as transport fuel has considerable environmental benefits. The quantity of LNG is traded on the basis of energy transferred, calculated from volume, density and gross calorific value. High-speed, accurate density measurement is therefore of significant commercial value.

The electrical capacitance tomography (ECT) device described in this paper has the potential to measure the LNG density rapidly, on-line at a moderate cost. Continuous monitoring of variation in LNG density during dynamic LNG flow measurement also gives a good indication of change in fluid quality and thus onset of boiling which is known to affect measurement accuracy. ECT is a leading candidate to be explored for online density measurements through measurement of electrical permittivity, as in addition to average value, it offers the image of permittivity across the whole flow conduit, allowing localised bubbles, boiling or other variations to be identified and measured.

We report here experiments to explore the use of ECT in cryogenic applications. An 8-electrode test ECT sensor was designed, built and tested in laboratory conditions and then in liquid nitrogen. The resolution and imaging capability in cryogenic conditions are shown to be comparable to that under laboratory conditions. The experiments reported here use liquid nitrogen as an analogue fluid, but the results presented are believed to be representative of many cryogenic fluids. Although the use of ECT has been widely reported in the literature for multiphase flows in general, its use has not previously been reported for cryogenic flows. This paper offers proof of principle for ECT cryogenic multi-phase density and flow measurement.

Dielectric constant is strongly linked to fluid density, and the ECT sensor design tested here shows an estimated measurement of the relative permittivity of liquid nitrogen of 1.45 with a standard measurement error of 0.034. Measurement stability at cryogenic conditions gave an rms variation of output under static conditions of better than 0.001 relative permittivity units even though it was unguarded and only a single electrode ring. The primary errors are associated with the unguarded nature of the test sensor, which was primarily designed as a proof of concept and material demonstrator.

In addition, such an ECT sensor would provide clear images of any gas in the liquid and give a good estimation of the concentration and velocity of the gas bubbles. The scope of this work is to provide a proof of concept of the cryogenic ECT sensor.

1. Introduction

The use of Liquefied Natural Gas (LNG) as fuel has generated much interest in the global energy sector due to two main attractive drivers; the environmental benefits and the lower cost relative to other fuels. The global LNG custody transfer market has grown at a strong pace in the last decade (>4%) as can be inferred from the GIIGNL 2018 and 2019 annual reports [1,2].

The quantity of LNG is currently traded on the basis of energy transferred (i.e. energy content). The energy content is calculated from

* Corresponding author at: Atout Process Ltd, Ardearn, Wilverley Road, New Milton BH25 5TX, UK.
E-mail addresses: andrew_hunt@atoutprocess.com (A. Hunt), ad1696@coventry.ac.uk (I. Rusli), mschakel@vsl.nl (M. Schakel), asaad.kenbar@tuv-sud.co.uk (A. Kenbar).

https://doi.org/10.1016/j.cryogenics.2020.103207
Received 30 June 2020; Received in revised form 28 September 2020; Accepted 8 October 2020
Available online 24 October 2020

LNG volume, density and gross calorific value. The density and gross calorific value are obtained from the measurement of LNG composition by analysing a vaporised LNG sample using gas chromatography [3].

The GIIGNL handbook [3] estimates an uncertainty in the measured LNG energy transferred ranging between 0.50% and 0.74% ($k = 2$). Given the current size of the global LNG custody transfer market of about 70 billion euro's, a 1% uncertainty in measured LNG energy content corresponds to a financial risk of about 700 million euros. The estimated uncertainty stems from the combined measurement uncertainty from volume (0.20% to 0.54%; $k = 2$), density (0.46%; $k = 2$) and gross calorific value (0.04% to 0.08%; $k = 2$). Most of the challenges are associated with the measurement of LNG volume and density. In current industry practice where the LNG density is determined from the composition measurement, important uncertainty sources are the representative nature of the sample both in space and time, the choice of the correct equation of state, and the accuracy of temperature and composition measurements. The LNG industry would benefit from a reliable, and industry accepted, online and direct LNG density measurement, in which temperature and composition measurements are not required thus eliminating their contribution to the measurement uncertainty of the density.

A review of density calculation methods used in LNG custody transfer applications has been reported in [4]. Comparison of thirteen density calculation methods using open literature data for measured density showed that the method adopted by the LNG industry [5,6], namely revised Klosek and McKinley method (RKM) appeared to give best accuracy for LNG density calculation. The uncertainty of the RKM method was reported to be 0.1%. This uncertainty estimate is only valid for calculations around atmospheric pressure. At higher pressures, experimental data have demonstrated that the RKM method is less accurate [7].

Although, a primary densimeter developed by Ruhr University of Bochum (RUB) provides highly accurate SI-traceable measurements of LNG density with estimated uncertainty of 0.02% [8], it cannot be used in the field to measure the LNG density directly as it has been designed as a laboratory device suitable for density measurement of LNG samples or pre-prepared LNG mixtures. However, interest in development of accurate and cost-effective means for measuring LNG density directly and without the need for sampling is growing [9].

A different measurement device for analysing LNG composition based on direct analysis in the LNG transfer line(s) hence eliminating the need of an LNG sampling, vaporisation and gas analysis equipment, is being tested in a few pilot applications and known as the Raman spectroscopy method. Raman spectroscopy is an analytical technique that uses monochromatic light to excite and identify the vibrational modes of molecules. Each mode of each molecule generates a shift in the frequency of the scattered light. By analysing the frequency and intensity of the scattered light, the sample's composition may be determined. The scattering interaction is so short-lived that the measurement is independent of the flow rate of the sample [3]. When validated for LNG composition measurement, this method can potentially result in determination of LNG density with better uncertainty than the traditional method which requires a representative sampling technique.

One of the currently available devices for direct measurement of fluid density on-line is by using a Coriolis flow meter. Coriolis meters have been shown to measure density of fluids such as water and oils with good accuracy due to availability of reference calibration facilities. However, when used under cryogenic conditions, the current-industry practice is to calibrate the meter with water for mass flow rate and density and then transfer this calibration to cryogenic conditions using appropriate corrections. References [10,11] presented Coriolis flow meter calibrations at ambient and cryogenic conditions, however, no direct SI-traceable measurement of density under cryogenic conditions was performed as part of this work.

Recently, a cryogenic densimeter was developed based on the speed-of-sound measurement of cryogenic liquids [12], which could enable direct on-line measurement of LNG density. This densimeter has been tested in static mode with liquified methane of known density. The next step is to test the device in flowing conditions and compare its measured density with the density measured by a Coriolis flow meter.

Although there are, as described above, a number of candidate techniques for on-line density measurement, none are yet proven. Custody transfer is typically performed when LNG is transferred at pressure slightly higher than the ambient pressure (1 to 3 bar) and therefore the fluid is close to its boiling point. This means onset of boiling may occur when the ambient heat gain is sufficiently high resulting in two-phase flow. In the current industry standard flow metering techniques, flow and density measurements can be deemed inaccurate when two-phase flow occurs. It is therefore desirable to have a device that can directly identify and measure two-phase flow. The ECT device described in this paper has the potential to measure the LNG density rapidly, on-line at a moderate cost. ECT has not to the authors' knowledge been previously reported in this application.

This paper reviews the ECT methodology in relation to density measurement, describes the cryogenic ECT design, its algorithm, its operation, and a presentation of ambient and cryogenic test results, and relative permittivity measurements. The paper concludes with a forward view on the test sensor application in LNG flows.

2. Review of ECT and its application to density measurement

ECT enables imaging of the permittivity distribution of multiphase flows including gas–solid flows [13,14] and gas–liquid flows [15–17]. More recently, ECT has also been used to track propellant centre of mass (CoM) and determine propellant slosh forces [18]. The relative permittivity distribution is captured in a cross-section of the process flow, from which the relative concentration (volume ratio) of the components is calculated. When twin-plane ECT measurements are performed, it is also possible to determine flow velocities and flow rates [19].

In cryogenic applications, there is often a need to identify the potential phase change of the cryogen during a process [20]. In heavy lift launchers for space applications, for example, the presence of bubbles entering the fuel lines can lead to engine destruction [21]. Furthermore, gravitational effects have a noticeable effect on cryogenic flow structure when compared to terrestrial conditions [22]. Pressure variations known as geysers can lead to violent pressure fluctuations which could cause failures in cryogenic feed pipes [23].

Non-intrusive techniques, such as ECT, are favoured as the cryogenic fluid to be measured is unperturbed. An assessment of potential non-intrusive measurement techniques for multiphase cryogenic flows during tank sloshing of launchers and satellites has previously been reported, highlighting the advantages and limitations of capacitance-based techniques [24]. Capacitance-based measurements have been performed on gaseous and liquid nitrogen to observe the formation of bubbles and the state of the liquid/gas interface [25] and to measure the liquid holdup in a nearly-horizontal tube [26]. A capacitance-based measurement technique has also been developed to assess the void fraction in two-phase hydrogen flow [20]. In two-phase solid–liquid hydrogen, density and mass flow rate measurements have been performed using capacitance-based methods [27].

By using multiple electrodes and a sensitivity map, ECT extends the potential of capacitance-based measurements such as those presented in [25,26] to allow for the flow to be visualised, hence allowing the flow distribution to be more accurately determined. Capacitance measurements have been adopted in liquid nitrogen to monitor the onset of boiling [28]. ECT could also be used to validate more recent numerical models of volume fraction for gaseous and liquid nitrogen [29,30].

3. Design of single-ring ECT sensor

The prototype sensor is shown in Fig. 1, consisting of eight stainless

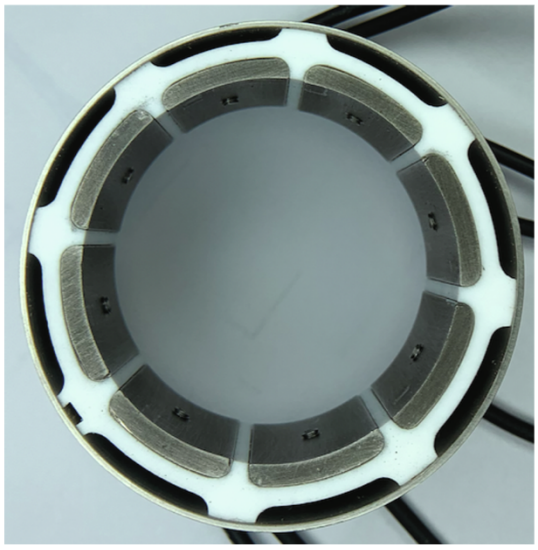

Fig. 1. Prototype ECT sensor for cryogenic applications, showing stainless steel electrodes, outer shell and PTFE insulation.

steel electrodes fitted in a 316-stainless-steel shield. This short sensor represents a section of a future full ECT sensor. A full sensor would have several of these rings along the length of the device in the flow direction, probably five sections operated as guard-sensor-guard-sensor-guard. Such an arrangement is described in reference [31] where it is shown that accurate measurements of permittivity distribution by ECT can be used to derive gas concentration profiles across the flow. Use of such sensors in LNG flows would allow profiles of permittivity to be measured, interpreted either as density changes in the liquid (when the changes are small) or as concentrations of gaseous phase when changes in permittivity are large. If there is a second phase present, such as when boiling occurs, the twin sensor plane arrangement can be used to measure cross-correlation velocity and hence flowrate.

This segment of an ECT flow sensor was designed to work at cryogenic temperatures, and for a typical 2″ (50.8 mm) industry standard pipe size. The sensor cables were standard coaxial SMB terminated cables. The internal bore of the sensor was 50.8 mm diameter, not corresponding to any particular pipe schedule, and made up of solid stainless steel electrodes with narrow separation zones of PTFE. The PTFE was chosen for its electrical insulating and mechanical properties, and while it may contribute to the thermal insulation of the sensor this was not a specific part of the design.

4. Imaging and calculation of sensitivity maps

Imaging from ECT measurements requires an inverse problem to be solved inferring from the measured capacitances the permittivity distribution within the sensor. The sensitivity map is derived from a forward model by calculation of the electric field between each independent pairing of electrodes. There are 64 pairings of electrodes possible for eight electrodes, but eight of these are 'self' measurements (1,1), (2,2) etc., while the remaining 56 are made up of two sets of reciprocal measurements (1,2) (2,1) etc. which are electrically identical so there are 28 independent capacitance measurement pairs. In the measurement system used here the reciprocal pairs are averaged to reduce noise. The cross-product of electric field between two driven electrodes is calculated to give each of the 28 lines of the sensitivity map. If $\boldsymbol{C}$ is the measured vector of 28 capacitance pairs and $\boldsymbol{K}$ is the permittivity distribution by pixel within the sensor then the forward model is:

$$\boldsymbol{C} = \boldsymbol{S}\cdot\boldsymbol{K} \tag{1}$$

$\boldsymbol{K}$ is an $m \times 1$ matrix containing the pixel permittivities, m is the number of pixels representing the sensor cross-section (eg 1024 for a 32 × 32 grid where 812 are 'active' within the circular sensor), and $\boldsymbol{S}$ is a 28 $\times m$ matrix containing the set of sensitivity matrices for each electrode-pair. The matrix $\boldsymbol{S}$ is commonly referred to as the sensitivity map of the sensor.

When making a set of measurements we have $\boldsymbol{C}$ as an input and are looking for $\boldsymbol{K}$, this we do through linear back-projection:

$$\boldsymbol{K} = \boldsymbol{S}^{\mathbf{T}}\cdot\boldsymbol{C} \tag{2}$$

$\boldsymbol{S}^{\boldsymbol{T}}$ is the transposed sensitivity map (formed by interchanging the rows and columns of the sensitivity map matrix $\boldsymbol{S}$). Although this is only strictly correct when $\boldsymbol{S}$ is non-singular, it is generally successful with ECT systems. Alternative inversions using Tikhonov or Landweber transforms are also possible. The sensitivity maps for each electrode pair were calculated using the Makemap* software from Atout Process Ltd who also supplied the full ECT measurement system. The voltage potential on a single electrode is shown in Fig. 2, while the equipotentials and lines of electric flux are shown in Fig. 3. The sensitivity map is calculated from the cross-product of the electric field of each of the electrodes in each independent pairing. Once the sub-maps are calculated for all of the four possible unique positions (shown in Fig. 4) the sub-maps for all of the 28 unique electrode pairs are simply rotations of the appropriate position.

The full sensitivity map is therefore a 28 × 812 matrix. Although this appears to be an under-defined system, flow structures are typically much larger scale than the pixels, so the limitation is not restrictive in practice.

5. Deriving permittivity and concentration

For future comparison with the cryogenic experiments the sensor was first used in air and full of polypropylene beads at ambient conditions as shown in Fig. 5 and further tests were carried out by inserting a plastic tube filled with beads as shown in Fig. 6. Because the test sensor contained only one ring of electrodes, completely unguarded, the electric field extended well outside the ends of the sensor and it was important to ensure that the measurement was not affected by what the sensor might be resting on.

The results of the room temperature measurements are shown in Table 1. The columns are arranged to represent capacitance pairs from different relative positions. In position 1 are those pairs alongside each other (1,2), (2,3), (3,4), (4,5), (5,6), (7,8), (8,1); position 2 are those next-but-one (1,3), (2,4), (3,5), (4,6), (5,7), (6,8), (7,1), (8,2); position 3 are next-but-two (1,4), (2,5), (3,6), (4,7), (5,8), (6,1), (7,2), (8,3); and position 4 are those across the pipe (1,5), (2,6), (3,7), (4,8). When the sensor is full of a material with uniform permittivity the position 4 measurements are close to those of a parallel plate capacitor so that the relative permittivity of the medium is determined from the simple equation:

$$K_{rel} = C_{high}/C_{low} \tag{3}$$

where K_{rel} is the relative permittivity of the material in the sensor when full, C_{high} is the measurement of capacitance at that fill, and C_{low} is the capacitance measurement when the sensor is empty.

The value of K_{rel} for the polypropylene beads can in principle be approximated from the ratio of any electrode pair with the sensor full and empty. However, due to the design of the sensor, the electrodes have a significant thickness in the radial direction, and so there is a contribution to the capacitance of side-by-side electrodes from the wall material, which does not change as the material inside the sensor is changed. By convention we use the across-the pipe values (position 4) as these are less affected by inhomogeneities in the measurement zone. The value thus derived is 1.718, there are no units as this is relative permittivity.

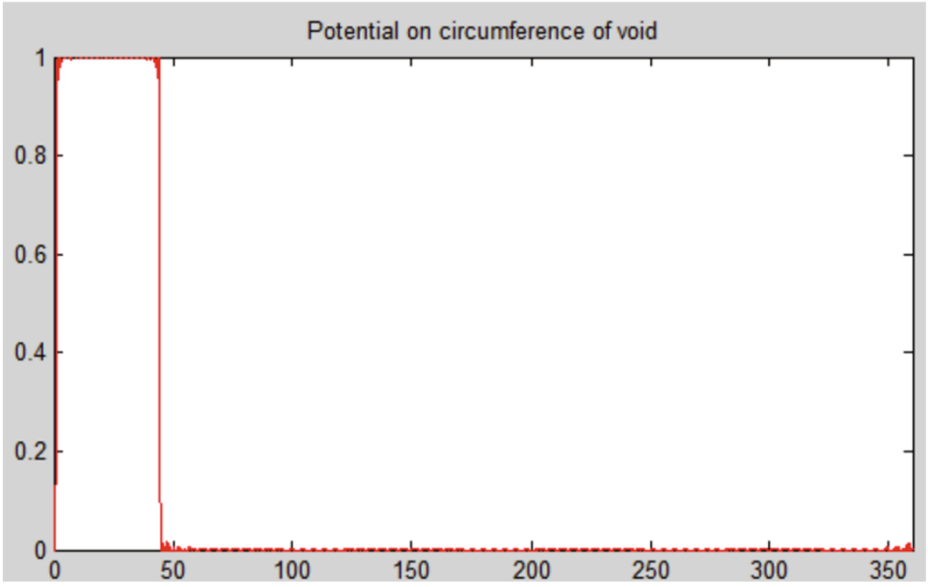

Fig. 2. Normalised potential applied to sensor wall (vertical axis), degrees around the perimeter (horizontal axis).

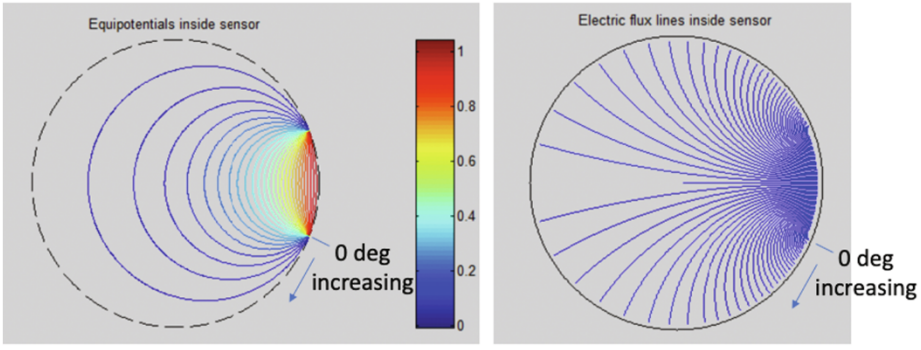

Fig. 3. Normalised equipotentials and electric flux lines for a single electrode.

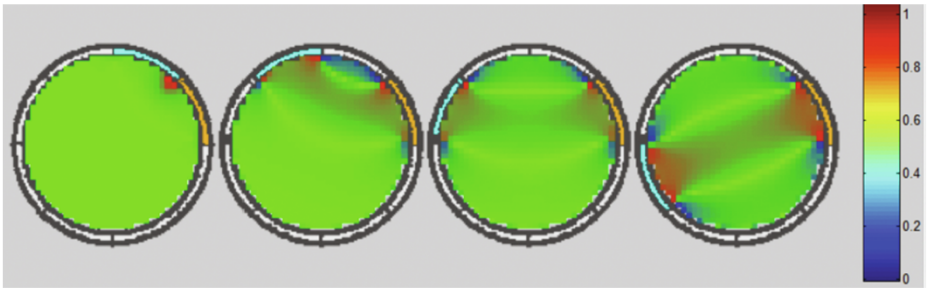

Fig. 4. Normalised sensitivity maps for each of the electrode pairs.

As shown in Fig. 6 a 21 mm plastic tube filled with polypropylene beads was inserted into the sensor and moved around. Concentration of the dispersed phase (in this case plastic beads) was calculated using the Maxwell model described in [31]. Concentration images at various times are shown in the upper part of Fig. 7. The red areas are the highest concentration while the blue shows the air background and the green areas represent the transition through a conventional RGB colour map. The white circle shows the size of the true tube. It can be seen that the images, despite being simple linear back projection as given in Eq. (2), are clear, with the size and location of the tube clear. There is a tendency for the image to 'smear' a little larger than the actual object (this can be corrected simply by adjusting the image parameters), and also for the image to 'run' to the side when close to the wall.

The mean concentration was calculated from the mean permittivity of all pixels using the series model [32], and this is shown in the lower part of Fig. 7. There is some variation as the tube is moved around, the mean value while the tube is not present is 1.0012 with rms variation of 0.0034, while the mean from measurements while the tube is present is 1.0936 with rms variation of 0.0068. For comparison the series model gives 1.105, a concentration difference of 1% of sensor full-scale reading.

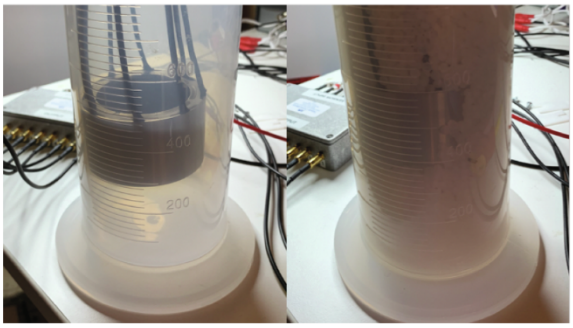

Fig. 5. Sensor suspended in a measuring cylinder, left empty, right filled with polypropylene beads.

Fig. 6. Plastic tube filled with polypropylene beads being inserted into sensor.

6. Cryogenic testing of single-ring ECT sensor

Cryogenic testing of the ECT sensor was performed using liquid nitrogen (LN2) in the experimental setup shown in Fig. 8 and Fig. 9. The sensor was placed on a thermally and electrically non-conducting spacer/holder inside a Pyrex bowl. Positioning the sensor on the spacer ensured that the sensor output was not influenced by the Pyrex bowl.

Prior to filling the bowl with LN2, existing air inside the plastic tank was purged with N2. This was done to remove all moisture inside the tank and prevent condensation from forming on the sensor. LN2 was then gradually introduced into the Pyrex bowl from the supply pipe, sufficient to submerge the sensor. Accurate rate control was not possible in this test but the fill time was around 2000 s. Capacitance measurements were continually made throughout the LN2 filling process.

Once the sensor was fully submerged in LN2, test runs were performed to see if the sensor was capable at capturing the presence of an electrically non-conductive material with a different permittivity to LN2 and what resolution of permittivity is possible. A plastic cylinder was used as the non-conductive material and was introduced into the sensor and moved around in the cross-section of the sensor while data was recorded.

To test for thermal shock, a second round of cryogenic testing was performed. In this test, decanted LN2 in a thermal flask was emptied into the Pyrex bowl containing the sensor while ECT readings were recorded.

7. Mean permittivity estimation

Throughout the experiments, the sensor generally remained functional under the tested cryogenic conditions. Substantial variations in output were seen as the LN2 boiled and as the sensor was filled at different levels and times.

The sensor fill profiles are shown in Fig. 10. The four subplots represent capacitance pairs from different relative positions as described in Table 1.

One of the electrodes suffered some loss of function through movement of one of the insulating pieces and the pairing (1,5), shown as the blue line in position 4 of Fig. 10, is not accurate. However, the remaining 3 cross-pipe pairs give the following values (see Table 2) for the times when the sensor was held stable full of LN2. These stable periods are shown in the figure within the red boxes (low - cold nitrogen) and high (liquid nitrogen). During the fill period from around 1000 s to 2800 s the signals are highly variable due to movement of liquid, vigorous boiling, and potential distortion of the sensor.

The mean value of relative permittivity given from Table 2 is 1.45. This compares well with values in the literature quoted between 1.43 and 1.47 [33,34].

8. Imaging performance of the test sensor at cryogenic conditions

To investigate the imaging performance of the sensor while at cryogenic conditions a plastic rod was inserted and removed repeatedly into and out of the LN2 filling the sensor. Mean permittivity measurements from the ECT analysis for the tests are shown in Fig. 11. The 'mean relative permittivity' shown on the y-axis is the mean of all pixels from the reconstructed image.

The inserted rod was hexagonal and 8.32 mm across flats, the cross-sectional area of plastic was 26.45×10^{-6} m^2 representing about 1.6% of the sensor area. As the plastic is PVC with a permittivity of 4, we would

Table 1
Capacitance values at room temperature, 28 independent measurements in fF for sensor full of air (first 7 rows) and full of polypropylene beads (second 7 rows). Columns show each successive pairing (1,2), (1,3), (1,4) etc, arranged to match the various independent positions shown in Fig. 1.

Position 1	Position 2	Position 3	Position 4	Position 3	Position 2	Position 1
978.843	33.168	17.177	14.672	17.069	32.381	977.371
968.680	32.852	17.435	14.349	16.949	32.719	
972.594	33.238	17.037	14.150	17.078		
966.428	32.619	16.877	14.175			
971.932	33.153	17.386				
950.665	32.012					
958.476						
1105.194	55.117	28.643	25.047	28.887	54.326	1118.225
1110.357	55.660	30.069	24.796	29.277	54.962	
1130.220	55.830	29.409	24.512	29.220		
1124.303	55.674	29.237	24.168			
1126.329	57.077	30.032				
1099.183	54.049					
1099.885						

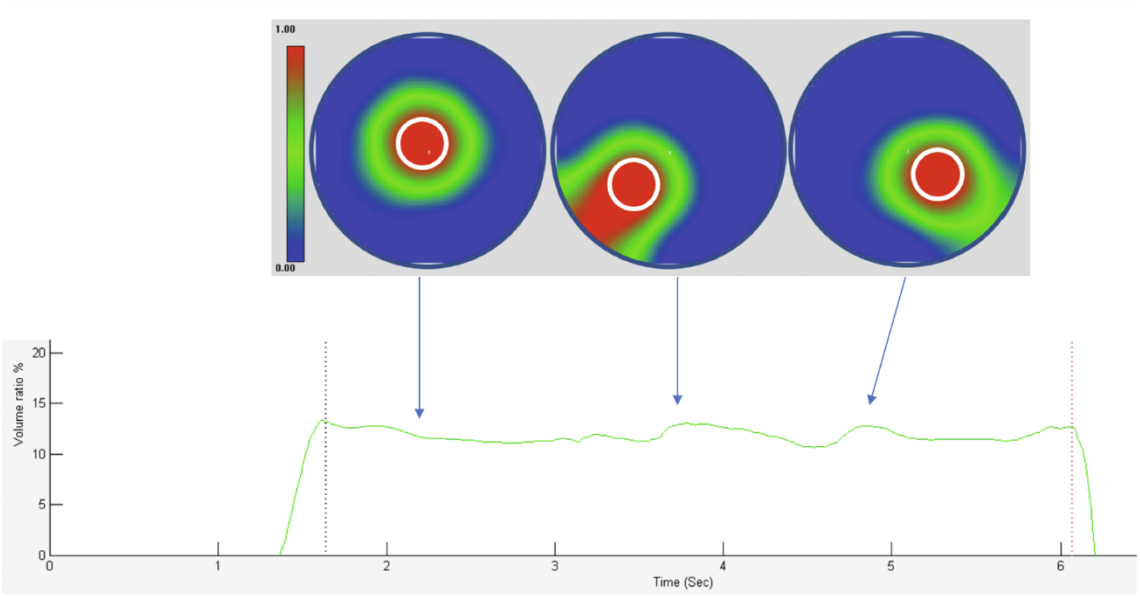

Fig. 7. Insertion of plastic rod, upper pictures show concentration images while lower picture shows average concentration against time.

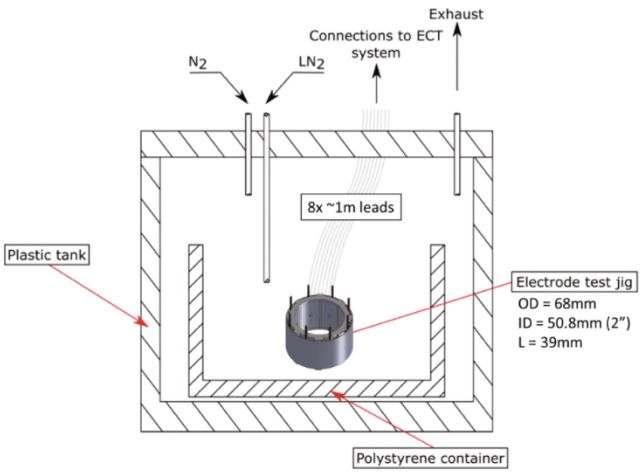

Fig. 8. Schematic of experimental setup of ECT sensor testing in liquid nitrogen (LN2).

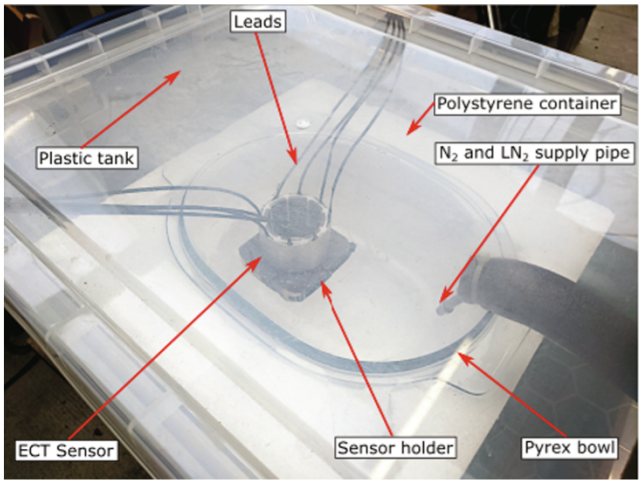

Fig. 9. Photo of experimental setup. In the photo, LN2 is being introduced into the Pyrex bowl.

expect to see an uplift to the measured in-situ permittivity of 0.0131 using the series model. From the figure it is clear that this is very close to the uplift seen. The mean level has been reduced slightly to 1.41, probably because the sensor is completely unguarded and the presence of the rod may be distorting the unguarded electric field. This source of error would not exist in the design of a full sensor.

On the third insertion of the rod it was moved around the sensor, so the variation seen will be dependent on any inaccuracies in the sensitivity map.

In summary, the expected uplift was 0.0131, the actual value 0.0122 (Table 3) a difference of 0.0009, while the rms variation over the periods with static conditions was 0.0004 to 0.0008 while the rms variation over periods with the rod moving was 0.0015. In addition, such an ECT sensor can give images of non-conducting inclusions in the flow as shown here, in real flows such inclusions could be gas bubbles.

9. Forward view: How to apply ECT in LNG and other cryogenic flows

This paper concentrates on measuring fluid density through permittivity. As noted in reference [35]:

"The dielectric constant of a fluid is closely related to its density through the Clausius-Mossotti (CM) function. In fact, dielectric constant measurement can serve as a simple and reliable substitute for density measurement". Thus, one primary application for ECT in measuring LNG is to give high-speed measurements of the distribution and average density across pipes or vessels containing the fluid.

Another application is measuring flowrate and flow structure when a cryogenic fluid is boiling or flowing as gas and liquid co-currently. ECT is an established technique for imaging of oil/gas 2-phase flows. The permittivity contrasts for oil/gas flows are larger than for cryogenic liquid/gas flows but still comparable, the ratio of liquid to gas permittivity in a typical oilfield flow is about 2, while for LNG it is around 1.6. ECT flowmeters may be constructed from several rings of electrodes, each ring being similar to that shown in Fig. 1 and tested here. Cross-correlation of signals between electrode rings spaced a small distance apart axially along the flow may be used to derive local flow velocities, which integrated with the measured concentration can derive flowrates for both phases (see [19]). Some examples results for the application of ECT to measure oil/gas flows are shown in Fig. 12 and Fig. 13, which were produced in research project MultiFlowMetII [36]. In each of the

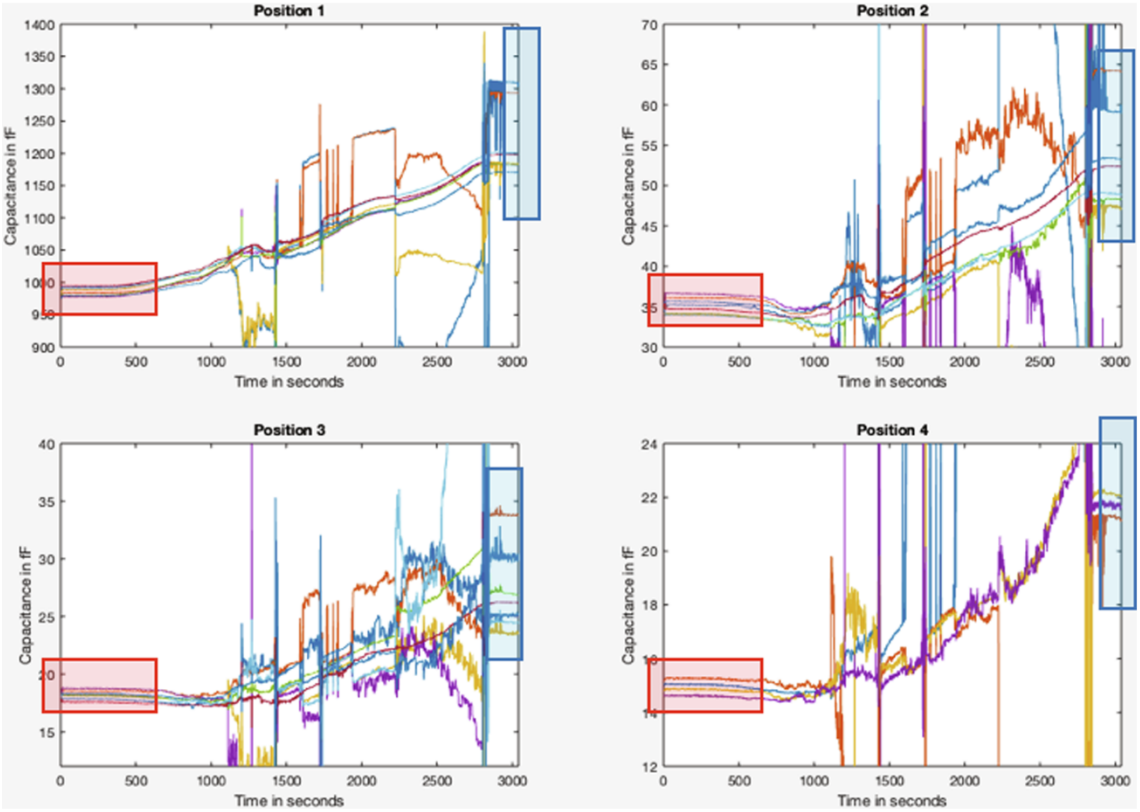

Fig. 10. Capacitance data over fill process - red boxes shows stable measurements while the sensor is full of gaseous Nitrogen, blue boxes show stable measurement with sensor full of LN2. (For interpretation of the references to colour in this figure legend, the reader is referred to the web version of this article.)

Table 2
Capacitance and relative permittivity of LN2.

Electrode pair	Capacitance with air	Capacitance full of LN2	Relative permittivity from ratio
(2,6)	15.3 fF	21.3 fF	1.39
(3,7)	14.9 fF	22.1 fF	1.48
(4,8)	14.6 fF	21.7 fF	1.48

figures sub-plot A shows a time-based stacked image of centreline pixel concentration values while sub-plot B shows a cross-sectional image of pixel concentration values for the last frame in A. Each of the images uses a colour scale where red represents gas and green represents oil, with the intensity varying based on concentration. Sub-plot C shows concentration of the two phases over the same timescale as A, while sub-plot D shows instantaneous flowrate as calculated from the images.

These examples of use of ECT to generate high-speed flow structure, density and concentration information could be widely applied in monitoring cryogenic fluids, and in particular LNG. Uncertainty on these measurements needs to be established through further experiments, but values better than 1% seem realistic based on previous published work [18].

10. Conclusions

In this work the primary objectives have been achieved:

Table 3
Mean and rms values of the different sections of the test in the previous figure.

Section	Mean uplift	rms
Sensor full LN2, no rod, all sections	0.000	0.0008
Sensor full LN2 + inserted rod – 1	0.0113	0.0004
Sensor full LN2 + inserted rod – 2	0.0138	0.0004
Sensor full LN2 + inserted rod – 3	0.0123	0.0015
Sensor full LN2 + inserted rod, all sections	0.0122	0.0005

Fig. 11. Rod insertion tests - mean permittivity against time.

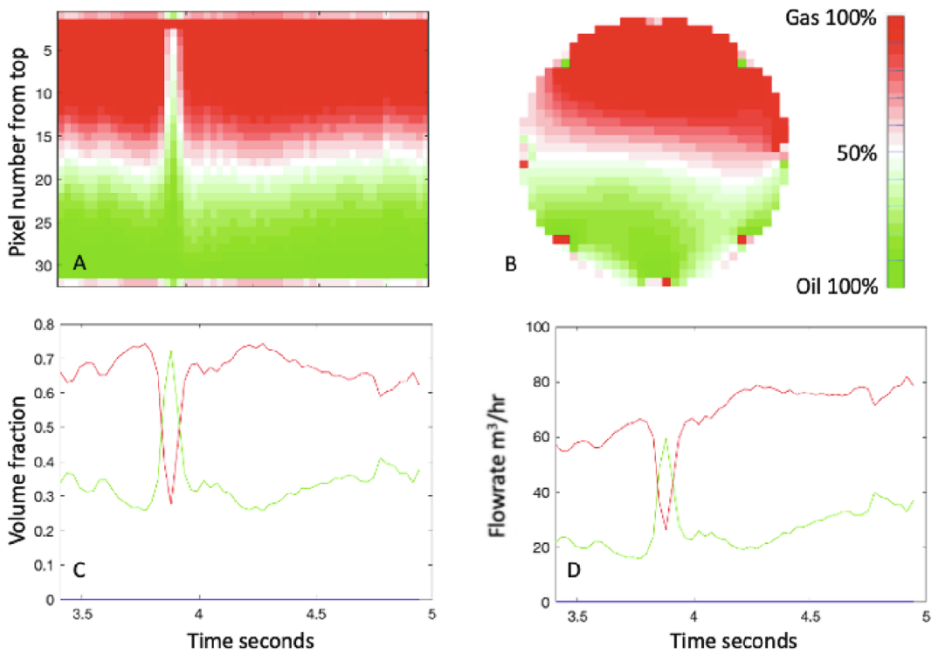

Fig. 12. Example flow information from ECT in multiphase flow. The reference average flowrates in the 2 min test were: oil 15 m^3/hr, gas 62 m^3/hr. Subplot D shows the flowrate estimated by ECT over a short period and so is not directly comparable with the reference. Time scale along x-axis for sub-plot A is the same as sub-plot C.

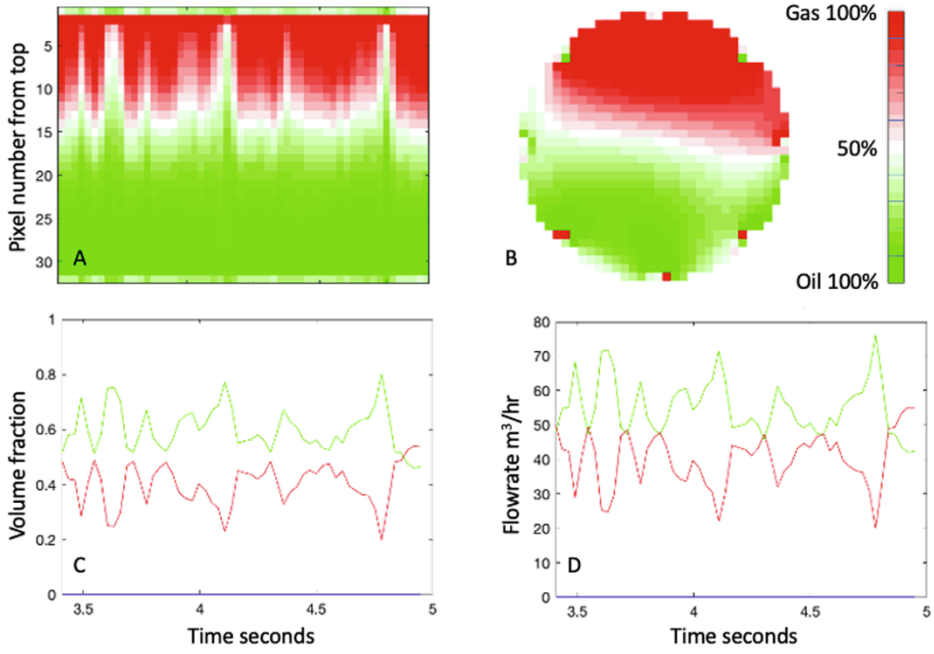

Fig. 13. Example flow information from ECT in multiphase flow. The reference average flowrates in the 2 min test were: oil 50 m^3/hr, gas 51 m^3/hr. Subplot D shows the flowrate estimated by ECT over a short period and so is not directly comparable with the reference. Time scale along x-axis for sub-plot A is the same as sub-plot C.

- ECT materials for cryogenic testing have been chosen,
- a single ring ECT sensor has been designed and tested,
- initial validation of ECT sensor and preliminary investigation into expected dominant uncertainty sources have been undertaken,
- proof of principle for ECT cryogenic multi-phase density and flow measurement has been established.

The ECT sensor design tested here shows an estimated measurement of the relative permittivity of LN2 of 1.45 with a standard measurement error of 0.034. Measurement stability at cryogenic conditions gave an rms variation of output under static conditions of better than 0.001 relative permittivity units even though it was unguarded and only a single electrode ring. The primary errors are associated with the unguarded nature of the test sensor, which was primarily designed as a proof of concept and material demonstrator.

In addition, such an ECT sensor would provide clear images of any gas in the liquid and give a good estimation of the concentration and velocity of the gas bubbles. Uncertainty on these values needs to be

established through further experiments on a sensor design, but values better than 1% seem realistic.

CRediT authorship contribution statement

Andrew Hunt: Conceptualization, Methodology, Software, Resources, Data curation, Supervision, Writing - original draft, Writing - review & editing. **Ijhar Rusli:** Methodology, Formal analysis, Investigation, Data curation, Writing - original draft, Visualization. **Menne Schakel:** Validation, Writing - original draft, Writing - review & editing, Project administration, Funding acquisition. **Asaad Kenbar:** Validation, Writing - original draft, Writing - review & editing, Project administration.

Declaration of Competing Interest

The authors declare that they are not aware of any competing interests, but note that Andrew Hunt is a director of Atout Process Ltd.

Acknowledgements

This work is part of the EMPIR 16ENG09 project 'Metrological support for LNG and LBG as transport fuel (LNG III)'. The LNG III project builds on two proceeding projects, LNG I [37] and LNG II [38]. This project has received funding from the EMPIR programme co-financed by the Participating States and from the European Union's Horizon 2020 research and innovation programme. Acknowledgements are also extended to McNaughton Dynamics for providing the testing facilities and TESCA consultancy for the design and manufacture of the ECT sensor. Results in the 'Forward view' section are from the EMPIR-funded project 16ENG07 MultiFlowMet II Multiphase flow reference metrology.

References

[1] International Group of Liquefied Natural Gas Importers. GIIGNL 2018 Annual Report, 2018. [Online]. Available: https://giignl.org/publications/giignl-2018-annual-report. [Accessed 30 May 2020].
[2] International Group of Liquefied Natural Gas Importers. GIIGNL 2019 Annual Report, 2019. [Online].
[3] International Group of Liquefied Natural Gas Importers. LNG Custody Transfer Handbook. 5th ed. Paris: International Group of Liquefied Natural Gas Importers; 2017.
[4] Kenbar A. Assessment of calculation Methods for LNG density using available reference density data, Houston, 2013.
[5] International Group of Liquefied Natural Gas Importers. LNG custody transfer handbook, 3rd ed. Paris: International Group of Liquefied Natural Gas Importers, 2011.
[6] BSI. Refrigerated light hydrocarbon fluids - measurement of cargoes on board LNG carriers. 1st ed. BSI; 2012.
[7] Tietz C, Richter M, Kleinrahm R, Span R. Report on the improvements of the selected EoS for calculation of the saturated liquid density of LNG. EMRP JRP ENG60 2016.
[8] Richter M, Kleinrahm R, Lentner R, Span R. Development of a special single-sinker densimeter for cryogenic liquid mixtures and first results for a liquefied natural gas (LNG). J Chem Thermodyn 2016;93:205–21.
[9] EURAMET. LNG III: Metrological Support for LNG and LBG as Transport Fuel, 2017. [Online]. Available: https://lngmetrology.info/lng-iii/. [Accessed 30 May 2020].
[10] Schakel M. Liquid Nitrogen Calibrations of Industry-Standard LNG Flow Meters used in LNG Custody Transfer, 20 December 2019. [Online]. Available: http://lngmetrology.info/wp-content/uploads/2020/01/Liquid-nitrogen-calibrations-of-industry-standard-LNG-flow-meters-used-in-LNG-custody-transfer_public_date_added.pdf. [Accessed 30 May 2020].
[11] Kenbar A, Schakel M. Calibration of industry-standard LNG flow meters under ambient and cryogenic test conditions. Flow Measur Instrument, 2020. [In preparation].
[12] Cavuoto G, Lago S, Giuliano-Albo PA, Serazio D. Speed of sound measurements in liquid methane (CH4) at cryogenic temperatures between (130 and 162) K and at pressures up to 10 MPa. J Chem Thermodyn 2020;142:106007.
[13] Hunt A, Pendleton JD, White RB. A novel tomographic flow analysis system. 3rd World congress on industrial process tomography, Banff. 2003.
[14] Romanowski A, Grudzien K, Williams RA. Analysis and interpretation of hopper flow behaviour using electrical capacitance tomography. Part Part Syst Char 2006;23(3–4):297–305.
[15] Hunt A, Pendleton J, Ladam Y. Visualisation of two-phase gas liquid pipe flows using electrical capacitance tomography, Manchester, 2004.
[16] Yang W, Li Y, Wu Z, Tsamakis D, Learmonth D, Xie C-G, et al. Multiphase flow measurement by electrical capacitance tomography. 2011 IEEE International conference on imaging systems and techniques, Penang. 2011.
[17] Ramli MF, Avila HEL, de Sousa FR, Tian W, Yang W. Multiphase flow measurement by electrical capacitance tomography and microwave cavity resonant sensor. 2019 IEEE international instrumentation and measurement technology conference (I2MTC), Auckland. 2019.
[18] Hunt A, Foster-Turner R, Drury R. Propellant slosh force and mass measurement. Int J Aerospace Eng 2018;3026872:2018.
[19] Toskey ED, Hunt A. Clamp-on subsea multiphase measurement. Offshore technology conference, Houston. 2015.
[20] Sakamoto Y, Peveroni L, Kobayashi H, Sato T, Steelant J, Rosaria Vetrano M. Void fraction measurement in cryogenic flows. Part I: design and validation of a void fraction capacitive sensor. Cryogenics 2018;94:36–44.
[21] Kandlbinder C, Fischerauer A, Mösch M, Helling T, Fischerauer G, Siegl M. Capacitive gas-phase detection in liquid nitrogen. J Sens Sens Syst 2017;6(1):135–43.
[22] Agarwal R, Dondapati RS. Numerical investigation on hydrodynamic characteristics of two-phase flow with liquid hydrogen through cryogenic feed lines at terrestrial and microgravity. Appl Therm Eng 2020;173.
[23] Mao H, Li Y, Wang L, Wang J, Xie F. Investigation of appearance and intensity of geyser phenomenon in a vertical cryogenic pipe. Int J Heat Mass Transf 2020;150.
[24] Poette C, Reynier P. Evaluation of 3D mapping experimental non-intrusive methods for multiphase flows. Int J Multiphys 2014;8(1):69–90.
[25] Kandlbinder C, Fischerauer A, Zürl T, Helling T, Fischerauer G. Observation of bubbles inside cryogenic liquids using capacitive multi-electrode, sensors. 2016 13th International Multi-Conference on Systems, Signals & Devices (SSD), Leipzig. 2016.
[26] Chen J, Wang Y, Zhang W, Qiu LZX. Capacitance-based liquid holdup measurement of cryogenic two-phase flow in a nearly-horizontal tube. Cryogenics 2017;84:69–75.
[27] Ohira K. Development of density and mass flow rate measurement technologies for slush hydrogen. Cryogenics 2004;44(1):59–68.
[28] Siegl M, Fischer A, Gerstmann J, Becker D, Schmidt K, Lindner G, et al. Advanced sensor technologies for cryogenic liquid propellant flow phenomena. 66th International Astronautical Congress 2015, Jerusalem. 2015.
[29] Xie H, Chen H, Gao X, Zheng X, Xiaoqin Z, Zhang X. Theoretical analysis of fuzzy least squares support vector regression method for void fraction measurement of two-phase flow by multi-electrode capacitance sensor. Cryogenics 2019;103.
[30] Xie H, Yu L, Zhou R, Qiu L, Zhang X. Preliminary evaluation of cryogenic two-phase flow imaging using electrical capacitance tomography. Cryogenics 2017;86:97–195.
[31] Hunt A, Abdulkareem LA, Azzopardi BJ. Measurement of dynamic properties of vertical gas-liquid flows. 7th International conference on multiphase flow ICMF 2010, Tampa. 2010.
[32] Process Tomography Ltd. AN2: Calculation of volume ratio for ECT sensors. www.tomography.com, 1999.
[33] Reesor GE, Dagg IR, Mohabir S. The complex dielectric constant of liquid nitrogen in the regiobn 18 to 26 GHz. Can J Phys 1975;53(23):2611–2.
[34] Edwards LG, Haberbusch M. Temperature and pressure effects on capacitance probe cryogenic liquid level measurements accuracy, NASA, 1993.
[35] Haynes WM, McCarty RD. Prediction of Liquefied Natural Gas (LNG) densities from new experimental dielectric constant data. Cryogenics 1983;23(8):421–6.
[36] Publishable Summary for 16ENG07 MultiFlowMetII Multiphase flow reference metrology, https://www.euramet.org/research-innovation/search-research-projects/details/project/multiphase-flow-reference-metrology/.
[37] EURAMET. LNG I: Metrology for Liquefied Natural Gas, JRP Protocol, 2010. [Online]. Available: https://lngmetrology.info/lng-i/. [Accessed 30 May 2020].
[38] EURAMET. LNG II: Metrological Support for LNG Custody Transfer and Transport Fuel Applications, 2014. [Online]. Available: https://lngmetrology.info/lng-ii/. [Accessed 30 May 2020].